ACS APPLIED MATERIALS & INTERFACES

Research Article

Cite This: ACS Appl. Mater. Interfaces 2017, 9, 44519−44528

www.acsami.org

Synergistic Effects between Doped Nitrogen and Phosphorus in Metal-Free Cathode for Zinc-Air Battery from Covalent Organic Frameworks Coated CNT

Zhongtao Li,[†] Weinan Zhao,[†] Changzhi Yin,[†] Liangqin Wei,[†] Wenting Wu,[†] Zhenpeng Hu,[*,‡] and Mingbo Wu[*,†]

[†]State Key Laboratory of Heavy Oil Processing, College of Chemical Engineering, China University of Petroleum (East China), Qingdao 266580, P. R. China

[‡]School of Physics, Nankai University, Tianjin 300071, P. R. China

Supporting Information

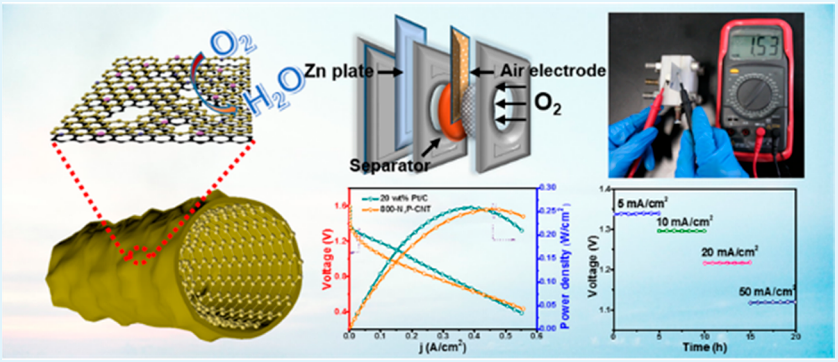

ABSTRACT: A covalent organic framework that is composed of hexachlorocyclotriphosphazene and dicyanamide has been coated on CNT to prepare metal-free oxygen reduction reaction catalyst through thermal polymerization of the Zn-air battery cathode. The N,P-codoped nanohybrids have highly porous structure and active synergistic effect between graphitic-N and -P, which promoted the electrocatalytic performance. The electrocatalysts exhibits remarkable half-wave potential (−0.162 V), high current density (6.1 mA/cm^{-2}), good stability (83%), and excellent methanol tolerance for ORR in alkaline solution. Furthermore, the N,P-codoped nanohybrids were used as an air electrode for fabrication of a high performance Zn-air battery. The battery achieves a high open-circuit potential (1.53 V) and peak power density (0.255 W cm^{-2}). Moreover, the effect of N,P codoping on the conjugate carbon system and the synergistic effect between graphitic-N and P have been calculated through density functional theory calculations, which are essentially in agreement with experimental data.

KEYWORDS: *oxygen reduction reaction, N,P-codoped, covalent organic framework, Zn-air battery, DFT calculation*

INTRODUCTION

Covalent organic frameworks (COFs) with high porosity and rigid chemical structures have widespread use in various fields,[1] such as gas storage,[2] hydrogen evolution,[3] proton conduction,[4] catalysis, and quantum sieving.[5,6] Among them, some low-band gap COFs exhibited extraordinary performance in organic electronics due to their semiconductivity and photoelectric effect, like field effect transistors, solar cells, light emission devices, and so forth.[7,8] These electronics polymers are generally composed by heterocyclics to lower the band gap through enlarged conjugation or donor−acceptor interactions, which possess 3D frameworks with large and polarized surfaces.[8] Some reports have explored COFs with heterocyclics as supports to coordinate and activate metal nanoparticles, resulting in composites with high electrocatalytic activities.[9,10] However, COFs derived from metal-free electrocatalysts have not been reported so far, which is due to the low stability chemical bonds under bias and limited charge transfer capability.

Recently, Zn−air batteries (ZABs) have attracted worldwide attention as a consequence of their large capacity, environmental benignity, cost-effectiveness, and safety.[11−15] However, the process of ZAB industrialization is hindered by expensive precious metal catalysts and sluggish kinetics of the ORR on cathode. Therefore, developing substitute cathode catalysts from earth-abundant elements with excellent catalytic activities is of great significance for applicable ZABs. Compared with platinum group metal catalysts for ORR, the metal-free electrocatalysts have undergone intense research due to their inherent advantages, such as wide availability of raw materials,

Received: September 29, 2017
Accepted: December 6, 2017
Published: December 6, 2017

DOI: 10.1021/acsami.7b14815
ACS Appl. Mater. Interfaces 2017, 9, 44519−44528

Scheme 1. Illustration of the Preparation of the N,P−C

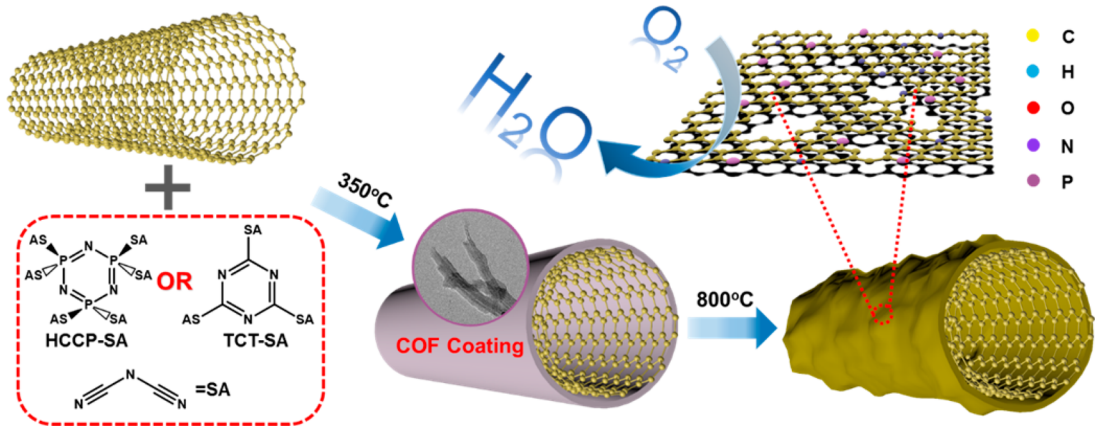

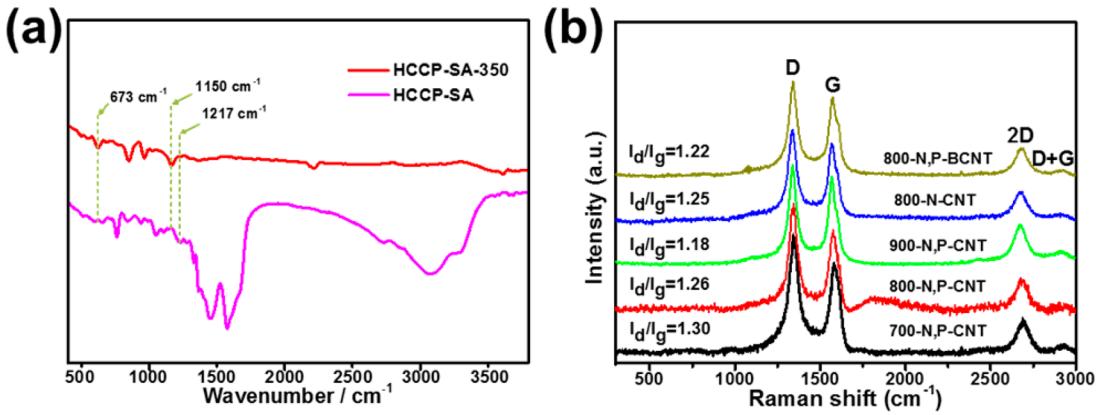

Figure 1. (a) FT-IR image of HCCP-SA, HCCP-SA-350. (b) Raman spectroscopy of 700-, 800-, 900-N,P-CNT, 800-N-CNT, and 800-N,P-BCNT.

environmental friendliness, and low cost.[16−19] Although heteroatom doped carbon catalysts (HDCs) exhibited great catalytic activity and stability among metal-free ORR catalyst,[20,21] the ORR performances of HDCs are still limited by inadequate mass and electron transfer and less active sites.[22] Generally, there are two strategies to promote the HDC catalytic performance: one is improving the porosities of HDCs to expose more active sites and accelerate mass transfer (often needing expansive templates and long procedures to create pores);[23] and the other is codoping carbon over two kinds of heteroatoms for more active sites through the synthetic effect (generally through thermal doping without control). However, the controllable synthesis of scaleable, template-free, and low-cost HDCs for ORR to substitute Pt/C is still met with great challenges.

To develop advanced metal-free electrocatalysts, the combination of heteroatoms containing porous COFs with conductive carbonic materials would bring special superiority to applicable HDCs.[24,25] The modular nature of COFs could potentially serve as unique components to controllably introduce heteroatoms and functional groups into the composites, which can promote catalytic activity through optimizing the interaction between delocalized conjugated π-electrons and oxygen. In addition, abundant cavities and the larger surface area of COFs would expose more active sites and accelerate mass transfer.[26]

In general, most self-sacrificing precursors could supply active N and P for doping through decomposition at high temperature. However, porous N,P-containing COFs are first thermally polymerized on a CNT surface at 350 °C, followed by high temperature cocarbonization for hetero doping, the procurement of which is composed of a conjugated cyclotriphosphazene core and six dicyanamide subunits in the periphery. And the COF-engaged synthesis method followed by higher temperature treatment for the heteroatom doped ORR catalyst possesses several advantages: (1) The N,P containing COF could uniformly coat the CNT which facilitates the good dispersal N and P doping to provide more catalytic active sites to facilitate the ORR process. (2) The formation of the COF structure could convert to more active N,P doped carbon, which would have a synergistic effect on promoting the ORR reaction. (3) The COF coating could separate CNTs to avoid their aggregation. Finally, a primary ZAB was constructed by as-prepared N,P-codoped ORR catalysts and showed excellent activity and durability, which could be due to the combination of the more active coating of porous COFs and high conductivity of CNT cores. To gain deeper understanding of the instrinsic codoped catalyst properties, density functional theory (DFT) calculation is performed to reveal the synergistic effects between doped N and P atoms, which could activate adjacent carbon through rearranging the electron distribution. Meanwhile, the enhanced highest occupied molecular orbital (HOMO) of the optimized catalyst can simultaneously increase interaction with O_2 and accelerate mass transfer to facilitate ORR.

DOI: 10.1021/acsami.7b14815
ACS Appl. Mater. Interfaces 2017, 9, 44519−44528

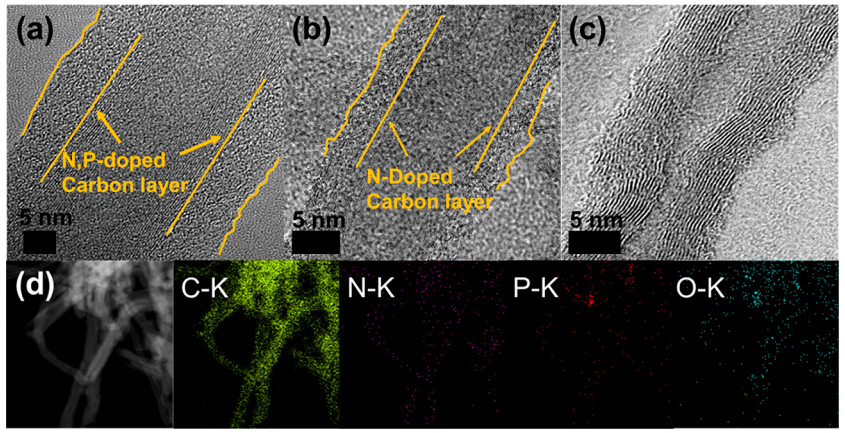

Figure 2. TEM image of (a) 800-N,P-CNT, (b) 800-N-CNT, and (c) 800-N,P-BCNT. (d) STEM-HAADF elemental mappings of C, N,P in 800-N, and P-CNT.

RESULTS AND DISCUSSION

As shown in Schemes 1 and S1 of the Supporting Information (SI), the precursor HCCP-SA was prepared first through nucleophilic substitution of hexachlorocyclotriphosphazene (HCCP) with sodium dicyanamide (SA), and the precursor HCCP-SA that is composed of conjugated heterocycles and unsaturated cyano substituents could cross-link with each other at 350 °C through the following reactions: (1) Open-ring reaction of HCCP to form conjugated polyphosphazenes;[27,28] (2) Trimerization between cyano groups in SA subunits to form conjugated triazine units.[29] As a result, the covalent organic structure would in situ polymerize on the surface of the carbon nanotube which could be proven by HRTEM imaging (Figure S1) . Then, the COF coating was thermally polymerized in depth to form a porous N,P-codoped layer on the CNT at 800 °C (namely 800-N,P-CNT). In order to investigate the relation between electrocatalyst activities and doping structure, 700-N,P-CNT and 900-N,P-CNT that were carbonized at 700 °C and 900 °C have been prepared. To better understand the effects of N,P-COF coatings on the growth of the electrocatalyst active sites and the synthetic effect between N,P atoms, the control samples, namely 800-N-CNT and 800-N,P-BCNT, were prepared following exactly the same process as that of 800-N,P-CNT with the exception of replacing HCCP-SA by cyanamide cyanuric (TCT) and barely HCCP, respectively.

Fourier transform infrared (FT-IR) spectra of HCCP-SA and HCCP-SA-350 were carried out to investigate the formation of N,P-COF, and N-COF during high temperature pyrolysis. As shown in Figure 1, HCCP-SA (purple line) shows a band at 1217 cm^{-1} belonging to the stretching vibrations of P═N.[30,31] After being thermally treated at 350 °C, the new bands of P−C and P−O stretching vibrations emerged at 673 and 1150 cm^{-1} in sample HCCP-SA-350 (red line), which revealed the ring-opening reaction of HCCP-SA and formation of the N,P-containing covalent organic cross-linked structure.[32,33] In addition, the final electrocatalysts of 700-, 800-, and 900-N,P-CNT were also tested in Figure S2a. The typical peaks of P−C and P−O vibration at 673 cm^{-1} and 1150 cm^{-1}, respectively, disappeared when the temperature reached 900 °C, which demonstrates that most of the P containing structure was cracked at high temperature. Furthermore, the TGA-DSC analysis of HCCP-SA and TCT-SA have been added in Figure S3. The most obvious enthalpy change in samples HCCP-SA and TCT-SA could be observed in 350 and 400 °C, which demonstrate the polymerization and formation of the COF structure. The weight loss over 400 °C could due to the gradual decomposition of the COF coating.

To investigate the structure of composition, X-ray diffraction of 700-, 800-, 900-N,P-CNTs, 800-N-CNT, and 800-N,P-BCNT are shown in Figure S2b. Two major peaks at 26.2° and 42.6° could be identified in five curves, which correspond to the diffraction peak of the (002) and (100) face of $\pi-\pi$ staked graphic carbon of CNT, respectively. Raman spectroscopy was used to further investigate the carbonization layer of 700-, 800-, 900-N,P-CNTs, 800-N-CNT, and 800-N,P-BCNT. In Figure 1b, all five samples displayed the peak at around 1344 cm^{-1}, 1574 cm^{-1}, 2672 cm^{-1}, and 2920 cm^{-1}, which exactly conformed to the D band, G band, 2D band, and D+G band, respectively.[34] In addition, the I_d/I_g ratio of 900-N,P-CNT (1.18) decreased with the increasing of pyrolysis temperature (700-N,P-CNT 1.30, 800-N,P-CNT 1.26), which reveal the increased degree of graphitization after higher temperature carbonization. Particularly, the I_d/I_g ratio of 800-N,P-CNT is comparable with 800-N-CNT (1.25) and 800-N,P-BCNT (1.22), which suggested that the temperature depended on a stacked conjugation structure.

The morphology and structure of the as-doped CNT are characterized by transmission electron microscopy (TEM). In Figure S1, the doped carbon coated structure is formed at 350 °C, which is composed of COF coatings and CNT cores. The morphology of the coating on the CNT is successive and uniform, which indicates the strong interaction between HCCP-SAs and CNT. After being heated up to 800 °C in Figure 2a, an N,P codoped carbon coated structure composed of a rough carbonized coating and CNT core could be identified in sample 800-N,P-CNT. The N,P-doped carbonic coating not only enlarged the surface area of the CNT, but also offered more active sites to accelerate the ORR process. In Figure 2b, 800-N-CNT displayed a similar carbon coated structure as 800-N,P-C with an N-doped carbonic coating on the surface of the CNT. In contrast, the coating on the CNT of 800-N,P-BCNT could hardly be identified in Figure 2c, which would be ascribed to the low thermal stability and lower polymerization ability of HCCP (hexachlorocyclotriphosphazene) without SA substitution. STEM-HAADF elemental mappings (Figure 2d) exhibit uniform distribution of C, N, P, and O elements in 800-N,P-CNT, which also demonstrates the successful and uniform doping of N and P onto CNTs.

DOI: 10.1021/acsami.7b14815
ACS Appl. Mater. Interfaces 2017, 9, 44519−44528

The intensively increased N_2 adsorption of all the catalysts under relatively high pressure (P/P_0 = 0.8−1.0) suggested the formation of macropores.[35] The Brunauer−Emmett−Teller (BET) surface area of the oxide multiwall CNT (101.3 m^2g^{-1}), 700-N,P-CNT (176.5 m^2g^{-1}), 800-N,P-CNT (181.9m^2g^{-1}), and 900-N,P-CNT (139.1 m^2g^{-1}) was obtained in Figures S4, S5, and S6 and Table 1. Compared with the oxide multiwalled carbon nanotube, the increased BET surface area and total pore volume of 700-N,P-CNT and 800-N,P-CNT would con\tribute to the formation of a COF layer on the carbon nanotube and the decomposed N-containing heterocycles, which would lead to more concave-convex features to increase surface area.

Table 1. N_2 Adsorption−Desorption Parameters of All Samples

sample	specific surface area (m^2 g^{-1})	pore volume (cm^3 g^{-1})	average pore size (nm)
800-N,P-CNT	181.9	1.26	16.43
700-N,P-CNT	176.5	1.03	14.79
900-N,P-CNT	139.1	0.82	17.44
800-N-CNT	151.4	0.95	16.87
800-N,P-BCNT	126.7	0.78	14.85
oxide CNT	101.3	0.72	9.12

Nevertheless, the surface area is obviously decreased at 900 °C, which is due to closer stacked graphitized carbon after the exhaustion of heteroatoms at higher temperature. As a control sample, the smallest BET surface area of 800-N,P-BCNT (126.7 m^2g^{-1}) revealed the poor doping ability of pure HCCP, which slightly changed the morphology of the CNT without COF modification. In contrast, 800-N-CNT that possessed a comparable BET (151.4 m^2g^{-1}) as N,P-CNT was ascribed to the formation of an N-doped COF structure. The Barrett−Joyner−Halenda (BJH) model was used in calculating the pore size distribution curves according to the desorption isotherm (Figures S4, S5, and S6.). 800-N,P-CNT possesses a large amount of mesopores with an average size at 2.55 nm (Figure S5b) and an H3-type hysteresis, which could also facilitate catalysis of ORR.

The XPS data suggest the chemical structure variation of the C, N, and P elements in different samples, which could be further confirmed by X-ray photoelectron spectra (Table S1). As shown in Table S1, Figure 3a (right axis), and Figure 3c (right axis), the quantity of N elements in N,P-CNTs are decreased (from 12.13% to 2.13%) with increasing doping temperature (from 700 °C, to 900 °C), which would due to decomposition of the less stable N-containing groups, leaving a porous structure that has also been verified by BET test. In the high resolution of N 1s spectrum (Figure 3b), three main absorbance peaks could be ascribed to pyridinic-N (398.6 eV), pyrrolic-N (400.5 eV), and graphitic-N (401.3 eV) respectively.[36] As shown in Figure S7a, even though the low carbonization temperature left the highest N contents in 700-N,P-CNT among all samples, the lowest content of pyridinic-N would finally deteriorate the catalytic activity.[37] Meanwhile, the increased pyridinic-N in 800- (Figure 3a,b) and 900-N,P-CNT

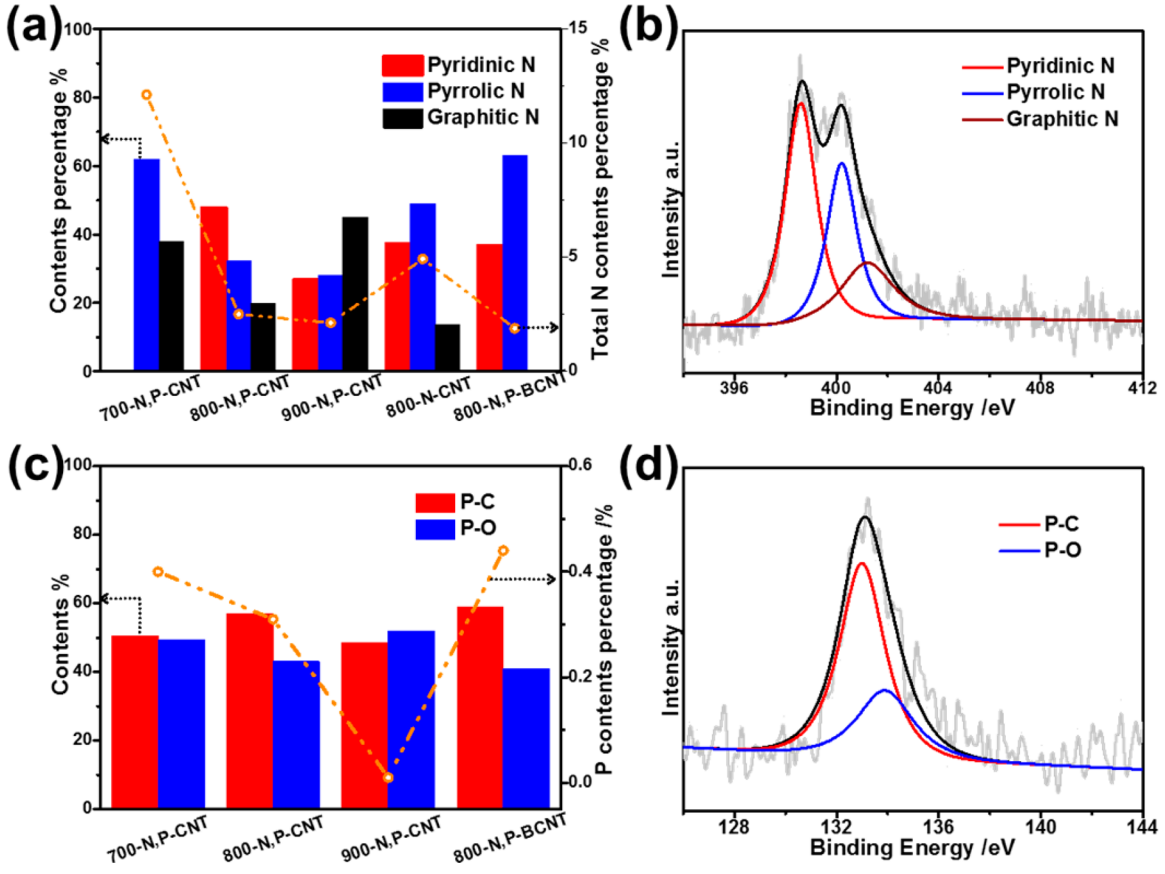

Figure 3. (a) The contents of pyridinic N, pyrrolic N, graphlitic N (left axis), and total N contents percentage (right axis) in 700-, 800-, and 900-N,P-CNTs. (b) High resolution N 1s signals of 800-N,P-CNT. (c) The P−C and P−O band contents percentage (left axis) and total P contents percentage in 800-N,P-CNT. (d) high resolution P 2p signals of 800-N,P-CNT.

DOI: 10.1021/acsami.7b14815
ACS Appl. Mater. Interfaces 2017, 9, 44519−44528

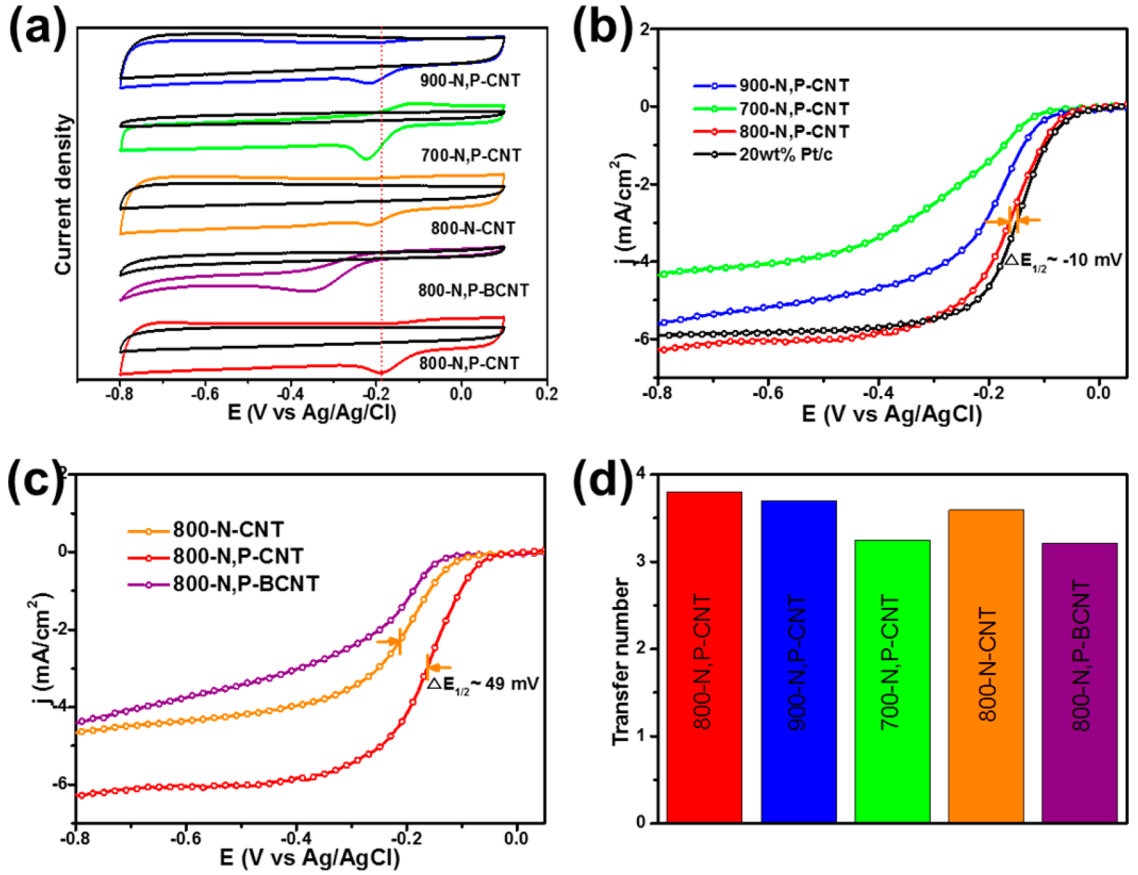

Figure 4. (a) CVs of T-N,P-CNT, 800-N-CNT, and 800-N,P-BC in N_2 and O_2 saturated 0.1 M KOH solution at a scan rate of 50 mV s^{-1}. (b) LSV curves of 700-, 800-, 900-N,P-CNT, and Pt/C at a rotation rate of 1600 rpm. (c) LSV curves of 800-N,P-CNT, 800-N-CNT, and 800-N,P-BCNT at a rotation rate of 1600 rpm. (d) Electron transition number of 700-, 800-, 900-N,P-CNT, 800-N-CNT, and 800-N,P-CNT.

(Figure S7b) demonstrates that the higher doping temperature could be beneficial to generate more active sites. In the control sample 800-N,P-BCNT (Figures 3a and S8b), none of the graphitic-N could be detected after thermal treatment without COF coating, due to unsubstituted HCCP without polymerizable dicyanamide subunits. In 800-N-CNT (Figure S8a), higher rates of pyridinic-N and graphitic-N were obtained after pyrolysis, which also indicated a large amount sp^2 hybridization N in the COF coating would favor being converted to pyridinic-N and graphitic N at high temperature.

Different from N, the content of P is stabilization when pyrolysis below 800 °C (700-N,P-CNT 0.41%, 800-N,P-CNT 0.31%, and 800-N,P-BCNT 0.44%), which reveals high stability of doped P from COF coatings. But, most P-doped structures are further cracked with pyrolysis at higher temperature (900 °C), which left 0.02% P residues in 900-N,P-CNT. The P 2p spectrum of N,P-CNTs (Figure 3d, Figure S7c, 8c) were deconvoluted into two peak at 133 and 134 eV, which correspond to P−C and P−O covalent bonding, respectively.[38] Furthermore, the structure and contents of P in N,P-CNTs with different pyrolysis temperature are shown in Figure 4c. 800-N,P-CNT possessed more P−C bands than other N,P-CNTs, which would generate more active sites. More electronegative P atoms could influence the charge distribution and geometric symmetry of the neighbor carbons, which could benefit accepting electron pairs on O_2 to accelerate ORR. 800-N,P-BCNT possesses similar P−C contents as that in 800-N,P-CNT except the lack of graphitic N and the content of P dramatically decreased in 900-N,P-CNT, all of which deteriorate their catalytic performance. Compared with 800-N-CNT, the doped P and graphitic N in 800-N,P-CNT have some synergistic effect to enhance ORR activity.

First, the electrocatalytic properties of catalysts were conducted by cyclic voltammetry (CV) in O_2 and N_2-saturated 0.1 M KOH solution, respectively. As shown in Figure 4a, a well-identified oxygen reduction peak could be observed between −0.20 V and −0.17 V in O_2-saturated electrolyte, but disappeared in the N_2-saturated electrolyte, suggesting the excellent oxygen reduction reaction electrocatalytic activity. Additionally, the cathodic peak of 800-N,P-CNT is more positive than that of other samples, which indicates the improved catalytic activity through synthetic effects between P−C and the graphitic N configuration.

The line scan voltammetry (LSV) of 800-N,P-CNT curves are shown in Figure 4b,c. A half-wave potential ($E_{1/2}$) at −0.162 V (versus Ag/AgCl) is achieved, which is only 10 mV more negative than that of the commercial Pt/C electrode. Furthermore, the limiting current density of 800-N,P-CNT was 6.1 mA/cm^2, which is even larger than that of commercial Pt/C. The corresponding LSV curves of 700-N,P−C and 900-N,P−C are included in Figure 4b for comparison; 900-N,P-CNT shows a lower half-wave potential (−0.201 V), and 700-N,P-CNT is the worst (−0.280 V). The highest half-wave potential and limiting current density of 800-N,P-CNT indicated that the proper temperature (i.e., 800 °C) led to doping of graphitic-N and phosphorus to provide more accessible activity sites through the synthetic effect. As confirmed in the XPS spectrum, a lower temperature (i.e.,

DOI: 10.1021/acsami.7b14815
ACS Appl. Mater. Interfaces 2017, 9, 44519−44528

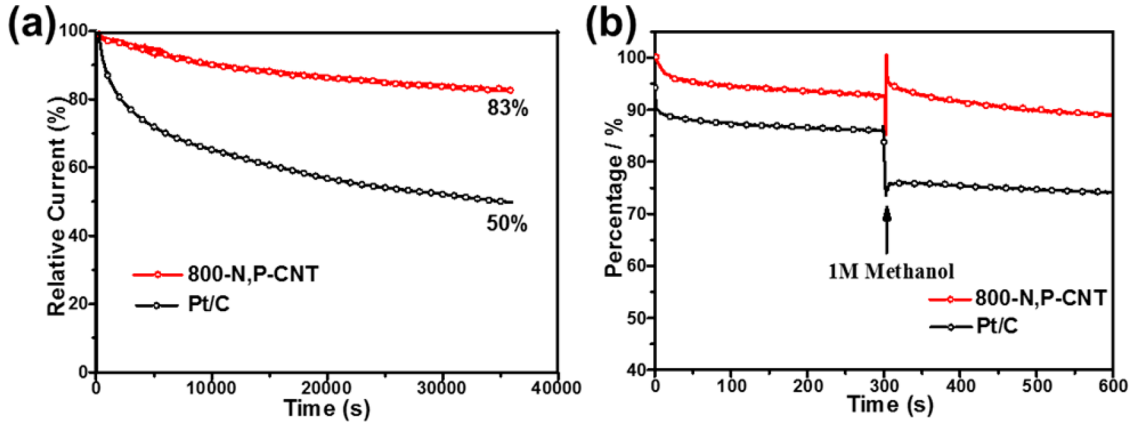

Figure 5. (a) Chronoamperometric response of 800-N,P-CNT and commercial Pt/C. (b) Chronoamperometric response of 800-N,P−C a constant potential in O_2-saturated 0.1 M KOH solution and electricity change with addition of methanol.

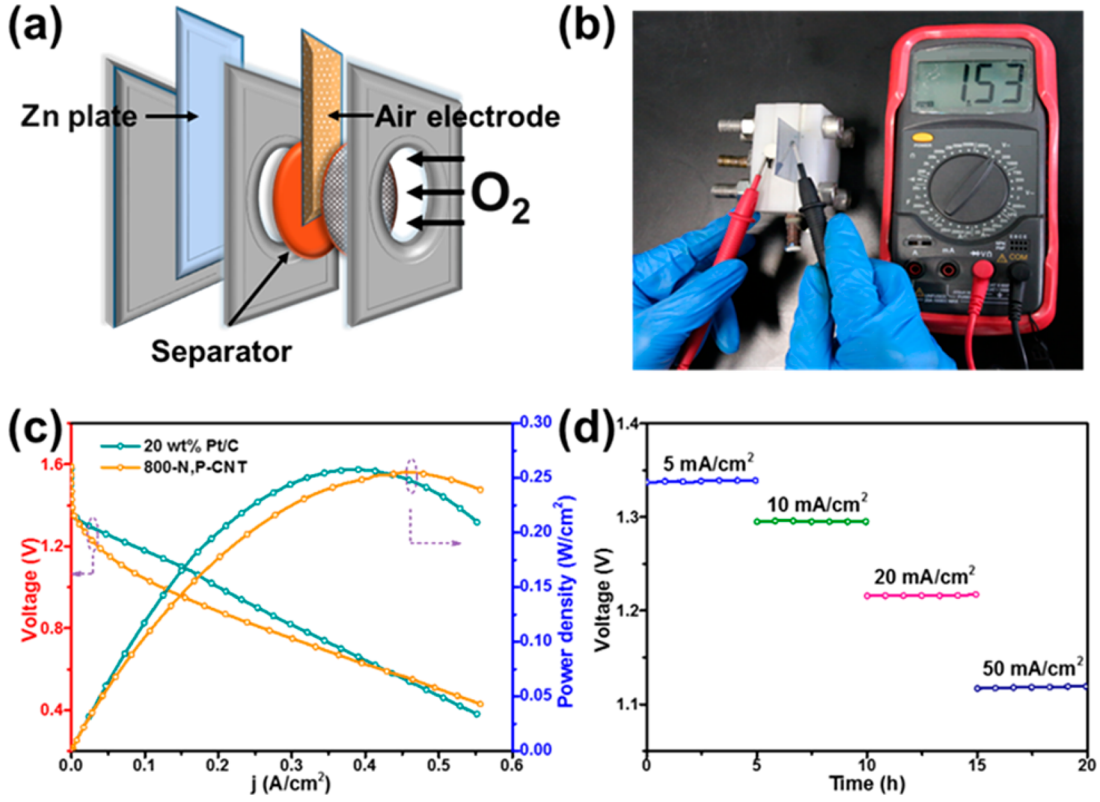

Figure 6. (a) Schematic of the basic configuration of a primary Zn−air battery. Photograph (b) of the ZABs and corresponding open-circle potential (OCP). The ZABs discharge polarization curves and power density of (c) 800-N,P-CNT, commercial Pt/C (the mass loading is 1 mg cm^{-1}). (d) Discharge curves at various current densities (5 mA cm^{-2}, 10 mA cm^{-2}, 20 mA cm^{-2}, and 50 mA cm^{-2}).

700 °C) would lead to more pyrrolic-N, which decreased the conductivity and activity of composition. In addition, the ORR performance of pure CNTs and N,P codoped carbon without CNTs were also be tested in Figure S11, the poor electrochemical activity of these samples demonstrates that both the high conductivity of the CNT and the synergistic effect between the doped N and P atoms play essential roles on promoting catalyst activity.

To further evaluate the catalytic activity of above sample, the rotating disk-ring electrode (RRDE) polarization curves were also gleaned at the electrode rotation speed of 1600 rpm (Figures S9 and S10) in O_2-saturated 0.1 M KOH solution. The peroxide yield of 800-N,P-CNT is less than 8% at the range of polarization procedure, correspondingly, the electron transfer number is calculated as $n \approx 3.8$ (Figure 4d), demonstrating its favorability to catalyze ORR through a four-electron ORR process as Pt/C. Meanwhile, the electron transfer numbers of 700-N,P-CNT, 900-N,P-CNT, 800-N-CNT, and 800-N,P-BC were also evaluated under the same conditions, which are calculated as 3.25, 3.7, 3.59, and 3.21, respectively (Figures S9 and S10). The lower transfer number of the above samples would attribute to the inefficient electron transmission process on the lower active surface to the kinetically sluggish ORR reaction. The electron transfer numbers of all samples were calculated through K-L equations. The diffusion-limited current density increased with the

DOI: 10.1021/acsami.7b14815
ACS Appl. Mater. Interfaces 2017, 9, 44519−44528

increasing rotation speed, which displayed a good linearity in the corresponding K-L plots. According to the K-L plots, the corresponding transfer electron number of 700-, 800-, 900-N,P-CNT, 800-N-CNT, and 800-N,P-BCNT were calculated to be 3.54, 4.0, 3.45, 3.32, and 3.27 at −0.5 V as shown in Figures S12 and S13.

As one of the key factors in ZABs, the stability of the catalysts was evaluated by chronoamperometric measurement in O_2-saturated 0.1 M KOH solution. As shown in Figure 5a, 800-N,P-CNT is obviously more stable than that of commercial Pt/C. After the 36 000 s test, 800-N,P-CNT remained at 83% of initial current density, while commercial Pt/C showed a 50% decrease in the initial current density under the same conditions. The remarkable durability would owe to the stable conjugated structure and electron-defect surface after doping on CNT. Moreover, methanol crossover is also nonnegligible in practical applications. The current density of 800-N,P-CNT has an almost negligible change when adding 1 M methanol in Figure 6b, while the Pt/C catalyst shows a sharp jump after injection due to the methanol oxidation progress, suggesting the excellent selectivity of 800-N,P-CNT and preferable methanol tolerance.

As a cathode material, the practical application performance of 800-N,P-CNT was investigated in the primary ZABs. In Figure 6a, the ZABs adopted a Zn plate as the anode without further purification, a carbon paper coated by electrocatalysts 800-N,P-CNT as the metal free cathode, and 6 M KOH as electrolyte. As shown in Figure 6b, ZABs with 800-N,P-CNT on the cathode possessed a high open-circuit potential (OCP) at 1.53 V. The discharge polarization curve showed that 800-N,P-CNT could achieve a maximum power density of ∼0.255 W cm^{-2} with a current density of ∼501 mA cm^{-2} (Figure 6c), which was close to or even higher than that of the commercial Pt/C catalyst (∼0.257 W cm^{-2} and ∼481 mA cm^{-2}). The preferable performances of 800-N,P-CNT due to the N,P-doped porous carbon structure, which provides high conductivity and facilitates the charge and mass transfer. Besides, the galvanostatic discharge method shows the discharge curve in different potential plain at various current densities (5 mA cm^{-2},10 mA cm^{-2}, 20 mA cm^{-2}, and 50 mA cm^{-2}). As shown in Figure 6d, there was not even a slight drop of 800-N,P-CNT in diverse discharge current densities, which indicated excellent stability of the cathode in ZABs. Furthermore, the long discharging time curve has been tested to evaluate the capacity and energy density of electrocatalysts. When normalized to the mass of consumed Zn, the 800-N,P-CNT could get a specific capacity of 762 mAh g^{-1} at 20 mA cm^{-1} (corresponding to an energy density of 922 Wh kg_{Zn}^{-1}) which achieved 93% utilization of the theoretical capacity (∼820 mAh $g^{-1}{}_{Zn}$) in Figure S14a. Even at a higher discharge rate (100 mA cm^{-1}), the battery could also exhibit remarkable specific capacity of 748 mAh $g^{-1}{}_{Zn}$ (corresponding to an energy density of 733 Wh kg_{Zn}^{-1}). To study the catalytic stability further, the EDS of 800-N,P-CNT after a prolonged discharge test is analyzed in Figure S14b. After a long time and a high discharge rate test, the content of N and P in electrocatalysts are slightly changed (2.1% of N and 0.18% of P), which could be attributed to a stable N,P-doped ORR catalyst.

Furthermore, first-principles calculations based on DFT methods were carried out to investigate the synergistic effect of pyridinic-, graphitic-N, and edge P (Gr, Py-N, P−C) in a simplified graphene model based on results of XPS. The pyridine-N and graphitic-N (Gr, Py−N-C), solo-P (P−C), P and pyridinic-N (Py-N,P−C) graphene (Figure S15−S18) were also calculated for comparison. Previous works demonstrated that carbon atoms with decreased charge density on defect and surrounded by heteroatom could serve as active sites of ORR, and the quantity of this type of carbon could be regarded as the indicator to evaluate the performance of the ORR process.[39−43] As shown in Figures S15b, S16b, S17b, and S18b, the Gr, Py-N,P−C possessed the minimum Mulliken charge of −0.824, and P−C was second lowest (−0.716). These data indicate that the doped P could intensely lower the Mulliken charge of the nearby carbon atoms due to its high electronegativity, which may result in enhancement of the catalytic activity. Besides, the electronic cloud distribution at the highest occupied molecular orbital (HOMO) of all four types of graphene-based models are also calculated (Figure 7, Table 2). Although the numeric

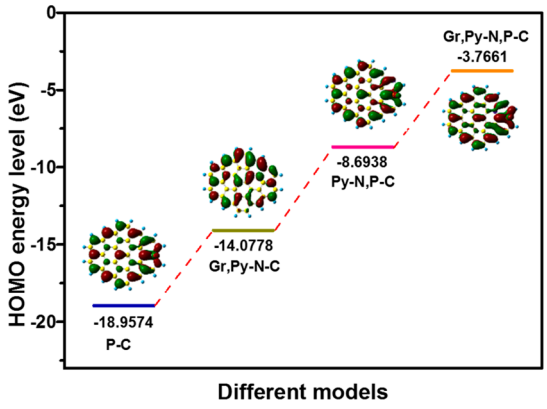

Figure 7. HOMO energy levels on four different models.

Table 2. HOMO Energy Level on Different Models and Other Reference Configuration

electrocatalyst	HOMO energy (eV)	adsorption energy (eV)	O−O band (Å)
Gr,Py-N,P−C	−3.7661	−0.656	1.495
Py-N,P−C	−8.6938	−0.463	1.472
Gr,Py-N-C	−14.0778	−0.272	1.314
P−C	−18.9574	−0.109	1.298

values seem to be very large due to the finite-size models used here, the trend of different dopants are clearly shown. According to the frontier molecular orbital theory, electron transfer should occur between the HOMO of electro-catalyst and the lowest unoccupied molecular orbital (LUMO) of O_2.[44,45] As the HOMO energy of the electro-catalyst goes higher, and the energy difference between it and the LUMO of triplet O_2 molecule becomes smaller, which makes it easier for the charge transfer process, decreases the overpotential, and accelerates the reduction of oxygen. Gr, Py-N, P−C possessed the highest HOMO energy (−3.7661 eV), indicating that heteroatom-doping of P and graphitic-N have a synergistic effect on promoting ORR reaction on the surface.

To evaluate the capability of the model for adsorbing O_2, several configurations for O_2 adsorption were considered and only the most stable one was taken for comparison among the different models. As an example, three configurations of O_2 adsorbed on Gr, Py-N, P−C were shown in Figure 8. The O−O band length of adsorbed O_2 and the adsorption energy (Table 2) clearly show that Gr, Py-N, P−C is better for capturing and activating the O_2 molecule than other N,P-doped

DOI: 10.1021/acsami.7b14815
ACS Appl. Mater. Interfaces 2017, 9, 44519−44528

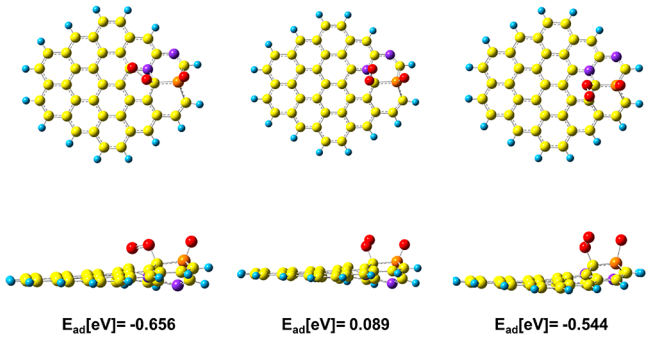

Figure 8. Different optimized structure (top and front sight) for O_2 adsorbed on Gr, Py-N, P−C, and corresponding adsorption energies.

graphene models. For the adsorption energy, among all models, Gr, Py-N, P−C has the largest one of −0.656 eV (minus for exothermic) and Py-N, P−C has the second largest one (−0.463 eV), which indicates the importance of graphitic N in N,P-codoping electro-catalysts. The O−O (the longer the more activity) bond in Gr, Py−P−C is spread up to 1.495 Å, indicating the easier ORR process than Py−N,P−C (1.472 Å).[46,47] On the basis of the results of experiments and calculations, the remarkable performance of ORR should come from the synergistic effect between P−C and graphitic-N. which could increase the HOMO energy of the COF and the interaction between O_2 and the material.

CONCLUSIONS

In summary, the metal-free nanocomposites for ZABs cathodes, which are derived from an N,P-codoped covalent organic framework with CNTs, have been systematically investigated. The high-performance catalysts have been synthesized by the cocarbonization of N,P-containing COF coated CNTs. In one aspect, the COF coating may play an essential role to accelerate mass and charge transfer to prompt the activity of ORR. In another aspect, the COF coating may also assist the formation of more active sites on the N,P-codoped structure. Both experimental results and theoretical calculations reveal that the enhanced ORR performance would be ascribed to the synergistic effect of graphitic-N and P in the nanocomposites. In a primary ZAB, the 800-N,P-CNT cathode exhibited comparable activity and improved stability compared to that of Pt/C cathode, which could be potentially used to develop low cost and applicable ZABs.

CALCULATIONS

Density functional theory (DFT) calculation has been carried out to investigate the effect of COF-derived N,P-dual doped electrocatalysts' active sites in ORR activity. All the calculations have employed the Gaussian 09 program. The B3LYP/6-31G+(d,p) level functional was used to calculate adsorption energies, and were corrected by BSSE.

The adsorption energy (E_{ad}) of the adsorbate was defined as the equation:O_2

$$E_{ad} = E(\text{structure} + O_2) - E(\text{structure}) - E(O_2) + E(\text{BSSE})$$

EXPERIMENTAL SECTION

Oxidation of Multiwall Carbon Nanotube. Multiwall carbon nanotubes were oxidized and purified first in mixed acid for nitric and sulfuric acid with a ratio of 1:1 for 10 h, then washed by DI water for several times, and dried at 60 °C for the next step.

Synthesis of HCCP-SA, TCT-SA. 0.696g HCCP and 1.068g SA were dissolved in 150 mL DMF and ultrasonic 1 h to mix uniformity, and then were transferred into an 80 mL Teflon-lined stainless-steel autoclave and maintained at 160 °C for 12 h. After the autoclave cooled to room temperature, the composite was centrifuged, washed by water and ethanol several times, and dried at 60 °C for further use.

Synthesis of 700-, 800-, 900-N,P-CNT. 50 mg prepared oxide multiwall carbon nanotube and 200 mg HCCP-SA were dispersed in a 50 mL methanolic solution and well sonificated. After drying at room temperature for 12 h, the composite was subjected to pyrolysis at 350 °C for 2 h and heated to a desired temperature at a heating rate of 5 °C min^{-1} under N_2 atmosphere for 2 h. The catalysts obtained at 700, 800, and 900 °C were noted as 700-N,P-CNT, 800-N,P-CNT, and 900-N,P-CNT, respectively.

Synthesis of 800-N-CNT and 800-N,P-BCNT. For comparison, the 800-N-CNT was prepared under same conditions, replacing HCCP-SA with TCT-SA (200 mg). 800-N,P-BCNT was synthesized from pyrolysis of the mixture of HCCP (200 mg) and CNT (50 mg).

Electrode Preparation and Electrochemical Measurements. Electrochemical measurements were conducted using 760E Bipotentiostat (CH Instruments). The ORR activity was carried out on a three-electrode system, including a glassy carbon (4 mm) as working electrode, a Pt column as counter electrode, and an Ag/AgCl as reference electrode. All the potentials were valued versus Ag/AgCl and were not *iR*-corrected. Typically, 2 mg catalysts mixed with 10 μL 5 wt % Nafion solution were dispersed in 800 μL of ethanol solution and sonicated for 30 min to form a homogeneous ink. Five μL catalyst ink was then dropped onto a glassy carbon electrode with a diameter of 4 mm (loading: 0.1 mg cm^{-2}). After purging with oxygen for 30 min, linear-sweep voltammetry was performed at a scan rate of 5 mV s^{-1} in 0.1 M KOH solution. A working electrode of 20 wt % commercial Pt/C (Johnson Matthey) was prepared in a similar manner. The loading amount of Pt/C was the same as that of other catalysts, i.e., 0.1 mg cm^{-2}. For the chronoamperometric test, the electrode was activated in O_2-saturated alkaline medium for one cycle, and then a static overpotential was fixed for a certain time to obtain the curve of time dependence of the current density. For the methanol crossover study, the current was recorded at −0.5 V vs Ag/AgCl with a rotation rate of 1600 rpm, with 0.1 M methanol added into the O_2-saturated electrolyte around 300 s. for the RRDE measurement, catalyst inks and electrodes were prepared by the same method as that of the RDEs. The ring potential was constant at 0.5 V vs Ag/AgCl. The % HO_2^- and electron transfer number (n) were determined by the following equation:

$$\%HO_2^- = 200 \times \frac{\frac{I_r}{N}}{I_d + \frac{I_r}{N}}$$

$$n = 4 \times \frac{I_d}{I_d + \frac{I_r}{N}}$$

where I_d is disk current density, I_r is ring current density, and N is collection efficient (N) of Pt ring. N is determined to be 0.40 from the reduction of $K_3Fe(CN)_6$.

The transfer electron number (n) was also calculated by the Koutechy−Levich (K−L) equation:

$$\frac{1}{J} = \frac{1}{J_L} + \frac{1}{J_K} = \frac{1}{B\omega^{1/2}} + \frac{1}{J_K}$$

$$B = 0.62nFC_0(D_0)^{2/3}\vartheta^{-1/6}$$

where J, J_K, and J_L are the measured current density, the kinetic current density, and diffusion limiting current density, respectively, ω is the rotation rate, n is the number of transferred electron per oxygen molecule, F is the Faraday constant (F = 96485 C mol^{-1}), C_0 is the concentration of O_2 in 0.1 M KOH (1.2×10^{-3} mol L^{-1}), D_0 is the diffusion coefficient of O_2 in 0.1 M KOH (1.93×10^{-5} cm^2 s^{-1}), and ϑ is the kinetic viscosity of the electrolyte in 0.1 M KOH solution (0.01 cm^2 s^{-1}).

DOI: 10.1021/acsami.7b14815
ACS Appl. Mater. Interfaces 2017, 9, 44519−44528

Preparation of Zn-Air Battery. The air electrode was prepared by uniform coating the prepared catalyst ink in the ORR process onto carbon paper and drying it in air. A Zn plate was used as anode and 6 M KOH aqueous solution used as electrolyte. The mass loading of electrocatalyst was 1 mg cm^{-2}. All electrodes were assembled into a homemade Zn-air test measurement.

Characterization. X-ray powder diffraction (XRD) patterns were collected on an X-ray diffractometer with Cu Kα radiation. Transmission electron microscopy and STEM-HAADF elemental mapping (TEM, JEM-2010UHR, Japan). The Raman spectra were measured on a Renishaw DXR Raman spectroscopy system with a 532 nm laser source. The Brunauer–Emmet–Teller (BET) specific surface area and pore size distribution were investigated by nitrogen adsorption–desorption isotherms on a sorption analyzer (Micromeritics, ASAP 2050, America). The elemental valences of the samples were analyzed using X-ray photoelectron spectroscopy (XPS, Thermo Scientific ESCALab250Xi).

■ ASSOCIATED CONTENT

Supporting Information

The Supporting Information is available free of charge on the ACS Publications website at DOI: 10.1021/acsami.7b14815.

Hypothetical synthesis mechanism, TEM, FT-IR images, XRD, TGA-DSC, BET, XPS, RRDE, Zn-air, and calculation results (PDF)

■ AUTHOR INFORMATION

Corresponding Authors

*E-mail: zphu@nankai.edu.cn (Z.H.).
*E-mail: wumb@upc.edu.cn (M.W.).

ORCID

Wenting Wu: 0000-0002-8380-7904
Zhenpeng Hu: 0000-0002-8469-1683
Mingbo Wu: 0000-0003-0048-778X

Notes

The authors declare no competing financial interest.

■ ACKNOWLEDGMENTS

This work was supported by the National Natural Science Foundation of China (21572269, 21302224, 21773124, and 21436003), and Fundamental Research Funds for Chinese Central Universities (17CX05015, 15CX08005A), Key Research and Development Program of Shandong Province, China (2017GGX40118), Qingdao Science and Technology Plan (15-9-1-108-jch), and Special Program for Applied Research on Super Computation of the NSFC-Guangdong Joint Fund (the second phase) under Grant No. U1501501. The calculations were performed on Tianhe II super computer in National Supercomputing Center at Guangzhou. The staff from the supercomputing center and the engineers from Beijing Paratera Technology Co., Ltd. provided efficient support to make the work perform smoothly.

■ REFERENCES

(1) Feng, X.; Ding, X.; Jiang, D. Covalent organic frameworks. *Chem. Soc. Rev.* **2012**, *41* (18), 6010.

(2) Furukawa, H.; Yaghi, O. M. Storage of Hydrogen, Methane, and Carbon Dioxide in Highly Porous Covalent Organic Frameworks for Clean Energy Applications. *J. Am. Chem. Soc.* **2009**, *131* (25), 8875–8883.

(3) Sprick, R. S.; Jiang, J.-X.; Bonillo, B.; Ren, S.; Ratvijitvech, T.; Guiglion, P.; Zwijnenburg, M. A.; Adams, D. J.; Cooper, A. I. Tunable Organic Photocatalysts for Visible-Light-Driven Hydrogen Evolution. *J. Am. Chem. Soc.* **2015**, *137* (9), 3265–3270.

(4) Chandra, S.; Kundu, T.; Kandambeth, S.; BabaRao, R.; Marathe, Y.; Kunjir, S. M.; Banerjee, R. Phosphoric Acid Loaded Azo (–N=N–) Based Covalent Organic Framework for Proton Conduction. *J. Am. Chem. Soc.* **2014**, *136* (18), 6570–6573.

(5) Ding, S.-Y.; Gao, J.; Wang, Q.; Zhang, Y.; Song, W.-G.; Su, C.-Y.; Wang, W. Construction of Covalent Organic Framework for Catalysis: Pd/COF-LZU1 in Suzuki–Miyaura Coupling Reaction. *J. Am. Chem. Soc.* **2011**, *133* (49), 19816–19822.

(6) Oh, H.; Kalidindi, S. B.; Um, Y.; Bureekaew, S.; Schmid, R.; Fischer, R. A.; Hirscher, M. A Cryogenically Flexible Covalent Organic Framework for Efficient Hydrogen Isotope Separation by Quantum Sieving. *Angew. Chem., Int. Ed.* **2013**, *52* (50), 13219–13222.

(7) Dogru, M.; Handloser, M.; Auras, F.; Kunz, T.; Medina, D.; Hartschuh, A.; Knochel, P.; Bein, T. A Photoconductive Thienothiophene-Based Covalent Organic Framework Showing Charge Transfer Towards Included Fullerene. *Angew. Chem., Int. Ed.* **2013**, *52* (10), 2920–2924.

(8) Waller, P. J.; Gándara, F.; Yaghi, O. M. Chemistry of Covalent Organic Frameworks. *Acc. Chem. Res.* **2015**, *48* (12), 3053–3063.

(9) Ren, S. B.; Wang, J.; Xia, X. H. Highly Efficient Oxygen Reduction Electrocatalyst Derived from a New Three-Dimensional PolyPorphyrin. *ACS Appl. Mater. Interfaces* **2016**, *8* (39), 25875–25880.

(10) Nandi, S.; Singh, S. K.; Mullangi, D.; Illathvalappil, R.; George, L.; Vinod, C. P.; Kurungot, S.; Vaidhyanathan, R. Low Band Gap Benzimidazole COF Supported Ni3N as Highly Active OER Catalyst. *Adv. Energy Mater.* **2016**, *6* (24), 1601189.

(11) Shinde, S. S.; Lee, C.-H.; Sami, A.; Kim, D.-H.; Lee, S.-U.; Lee, J.-H. Scalable 3-D Carbon Nitride Sponge as an Efficient Metal-Free Bifunctional Oxygen Electrocatalyst for Rechargeable Zn–Air Batteries. *ACS Nano* **2017**, *11* (1), 347–357.

(12) Lin, C.; Shinde, S. S.; Jiang, Z.; Song, X.; Sun, Y.; Guo, L.; Zhang, H.; Jung, J.-Y.; Li, X.; Lee, J.-H. In situ directional formation of Co@CoOx-embedded 1D carbon nanotubes as an efficient oxygen electrocatalyst for ultra-high rate Zn–air batteries. *J. Mater. Chem. A* **2017**, *5* (27), 13994–14002.

(13) Song, X.; Guo, L.; Liao, X.; Liu, J.; Sun, J.; Li, X. Hollow Carbon Nanopolyhedra for Enhanced Electrocatalysis via Confined Hierarchical Porosity. *Small* **2017**, *13* (23), 1700238.

(14) Lin, C.; Shinde, S. S.; Wang, Y.; Sun, Y.; Chen, S.; Zhang, H.; Li, X.; Lee, J.-H. Flexible and rechargeable Zn–air batteries based on green feedstocks with 75% round-trip efficiency. *Sustainable Energy Fuels* **2017**, *1* (9), 1909–1914.

(15) Shinde, S. S.; Yu, J.-Y.; Song, J.-W.; Nam, Y.-H.; Kim, D.-H.; Lee, J.-H. Highly active and durable carbon nitride fibers as metal-free bifunctional oxygen electrodes for flexible Zn–air batteries. *Nanoscale Horiz.* **2017**, *2* (6), 333–341.

(16) Zhou, M.; Wang, H. L.; Guo, S. Towards high-efficiency nanoelectrocatalysts for oxygen reduction through engineering advanced carbon nanomaterials. *Chem. Soc. Rev.* **2016**, *45* (5), 1273–307.

(17) Yang, M.; Hu, X.; Fang, Z.; Sun, L.; Yuan, Z.; Wang, S.; Hong, W.; Chen, X.; Yu, D. Bifunctional MOF-Derived Carbon Photonic Crystal Architectures for Advanced Zn-Air and Li-S Batteries: Highly Exposed Graphitic Nitrogen Matters. *Adv. Funct. Mater.* **2017**, *27* (36), 1701971.

(18) Jiao, L.; Zhou, Y.-X.; Jiang, H.-L. Metal–organic framework-based CoP/reduced graphene oxide: high-performance bifunctional electrocatalyst for overall water splitting. *Chem. Sci.* **2016**, *7* (3), 1690–1695.

(19) Cai, G.; Zhang, W.; Jiao, L.; Yu, S.-H.; Jiang, H.-L. Template-Directed Growth of Well-Aligned MOF Arrays and Derived Self-Supporting Electrodes for Water Splitting. *Chem.* **2017**, *2* (6), 791–802.

(20) Yang, S.; Peng, L.; Huang, P.; Wang, X.; Sun, Y.; Cao, C.; Song, W. Nitrogen, Phosphorus, and Sulfur Co-Doped Hollow Carbon Shell as Superior Metal-Free Catalyst for Selective Oxidation of Aromatic Alkanes. *Angew. Chem., Int. Ed.* **2016**, *55* (12), 4016–20.

DOI: 10.1021/acsami.7b14815
ACS Appl. Mater. Interfaces 2017, 9, 44519–44528

(21) Zhang, Z.; Sun, J.; Dou, M.; Ji, J.; Wang, F. Nitrogen and Phosphorus Codoped Mesoporous Carbon Derived from Polypyrrole as Superior Metal-Free Electrocatalyst toward the Oxygen Reduction Reaction. *ACS Appl. Mater. Interfaces* **2017**, *9* (19), 16236−16242.
(22) Lai, L.; Potts, J. R.; Zhan, D.; Wang, L.; Poh, C. K.; Tang, C.; Gong, H.; Shen, Z.; Lin, J.; Ruoff, R. S. Exploration of the active center structure of nitrogen-doped graphene-based catalysts for oxygen reduction reaction. *Energy Environ. Sci.* **2012**, *5* (7), 7936.
(23) Chen, Y. Z.; Wang, C.; Wu, Z. Y.; Xiong, Y.; Xu, Q.; Yu, S. H.; Jiang, H. L. From Bimetallic Metal-Organic Framework to Porous Carbon: High Surface Area and Multicomponent Active Dopants for Excellent Electrocatalysis. *Adv. Mater.* **2015**, *27* (34), 5010−6.
(24) Cai, S.-L.; Zhang, Y.-B.; Pun, A. B.; He, B.; Yang, J.; Toma, F. M.; Sharp, I. D.; Yaghi, O. M.; Fan, J.; Zheng, S.-R.; Zhang, W.-G.; Liu, Y. Tunable electrical conductivity in oriented thin films of tetrathiafulvalene-based covalent organic framework. *Chem. Sci.* **2014**, *5* (12), 4693−4700.
(25) Segura, J. L.; Mancheño, M. J.; Zamora, F. Covalent organic frameworks based on Schiff-base chemistry: synthesis, properties and potential applications. *Chem. Soc. Rev.* **2016**, *45* (20), 5635−5671.
(26) Jin, S.; Ding, X.; Feng, X.; Supur, M.; Furukawa, K.; Takahashi, S.; Addicoat, M.; El-Khouly, M. E.; Nakamura, T.; Irle, S.; Fukuzumi, S.; Nagai, A.; Jiang, D. Charge Dynamics in A Donor-Acceptor Covalent Organic Framework with Periodically Ordered Bicontinuous Heterojunctions. *Angew. Chem., Int. Ed.* **2013**, *52* (7), 2017−2021.
(27) Caminade, A.-M.; Hameau, A.; Majoral, J.-P. The specific functionalization of cyclotriphosphazene for the synthesis of smart dendrimers. *Dalton Trans.* **2016**, *45* (5), 1810−1822.
(28) Allcock, H. R. Ring-Opening Polymerization of Phosphazenes. *South African Med. J.* **1993**, *95* (12), 7719−7725.
(29) Jung, S. M.; Kim, D.; Shin, D.; Mahmood, J.; Park, N.; Lah, M. S.; Jeong, H. Y.; Baek, J. B. Unusually Stable Triazine-based Organic Superstructures. *Angew. Chem., Int. Ed.* **2016**, *55* (26), 7413−7.
(30) Zoghaib, W. M.; Husband, J.; Soliman, U. A.; Shaaban, I. A.; Mohamed, T. A. Analysis of UV and vibrational spectra (FT-IR and FT-Raman) of hexachlorocyclotriphosphazene based on normal coordinate analysis, MP2 and DFT calculations. *Spectrochim. Acta, Part A* **2013**, *105*, 446−55.
(31) Allaf, A. W. Gas-phase on-line generation and infrared spectroscopic investigations of polyphosphazenes, (NPX2)3 where X = F, Cl and Br. *Spectrochim. Acta, Part A* **2005**, *61* (7), 1499−503.
(32) Qu, K.; Zheng, Y.; Zhang, X.; Davey, K.; Dai, S.; Qiao, S. Z. Promotion of Electrocatalytic Hydrogen Evolution Reaction on Nitrogen-Doped Carbon Nanosheets with Secondary Heteroatoms. *ACS Nano* **2017**, *11* (7), 7293−7300.
(33) Dahl, K.; Sando, G. M.; Fox, D. M.; Sutto, T. E.; Owrutsky, J. C. Vibrational spectroscopy and dynamics of small anions in ionic liquid solutions. *J. Chem. Phys.* **2005**, *123* (8), 084504.
(34) Sadezky, A.; Muckenhuber, H.; Grothe, H.; Niessner, R.; Pöschl, U. Raman microspectroscopy of soot and related carbonaceous materials: Spectral analysis and structural information. *Carbon* **2005**, *43* (8), 1731−1742.
(35) Zhang, J.; Zhao, Z.; Xia, Z.; Dai, L. A metal-free bifunctional electrocatalyst for oxygen reduction and oxygen evolution reactions. *Nat. Nanotechnol.* **2015**, *10* (5), 444−52.
(36) Kong, X. K.; Chen, C. L.; Chen, Q. W. Doped graphene for metal-free catalysis. *Chem. Soc. Rev.* **2014**, *43* (8), 2841−57.
(37) Guo, D.; Shibuya, R.; Akiba, C.; Saji, S.; Kondo, T.; Nakamura, J. Active sites of nitrogen-doped carbon materials for oxygen reduction reaction clarified using model catalysts. *Science* **2016**, *351* (6271), 361−5.
(38) Chai, G.-L.; Qiu, K.; Qiao, M.; Titirici, M.-M.; Shang, C.; Guo, Z. Active sites engineering leads to exceptional ORR and OER bifunctionality in P,N Co-doped graphene frameworks. *Energy Environ. Sci.* **2017**, *10* (5), 1186−1195.
(39) Jia, Y.; Zhang, L.; Du, A.; Gao, G.; Chen, J.; Yan, X.; Brown, C. L.; Yao, X. Defect Graphene as a Trifunctional Catalyst for Electrochemical Reactions. *Adv. Mater.* **2016**, *28* (43), 9532−9538.
(40) Jiao, Y.; Zheng, Y.; Jaroniec, M.; Qiao, S. Z. Origin of the electrocatalytic oxygen reduction activity of graphene-based catalysts: a roadmap to achieve the best performance. *J. Am. Chem. Soc.* **2014**, *136* (11), 4394−403.
(41) Zhao, Y.; Yang, L.; Chen, S.; Wang, X.; Ma, Y.; Wu, Q.; Jiang, Y.; Qian, W.; Hu, Z. Can boron and nitrogen co-doping improve oxygen reduction reaction activity of carbon nanotubes? *J. Am. Chem. Soc.* **2013**, *135* (4), 1201−4.
(42) Zhu, Y. P.; Jing, Y.; Vasileff, A.; Heine, T.; Qiao, S.-Z. 3D Synergistically Active Carbon Nanofibers for Improved Oxygen Evolution. *Adv. Energy Mater.* **2017**, *7* (14), 1602928.
(43) Liang, J.; Jiao, Y.; Jaroniec, M.; Qiao, S. Z. Sulfur and nitrogen dual-doped mesoporous graphene electrocatalyst for oxygen reduction with synergistically enhanced performance. *Angew. Chem., Int. Ed.* **2012**, *51* (46), 11496−500.
(44) Fukui, K. The Role of Frontier Orbitals in Chemical Reactions (Nobel Lecture). *Angew. Chem., Int. Ed. Engl.* **1982**, *21* (11), 801−809.
(45) Li, L.; Wei, Z.; Chen, S.; Qi, X.; Ding, W.; Xia, M.; Li, R.; Xiong, K.; Deng, Z.; Gao, Y. A comparative DFT study of the catalytic activity of MnO 2 (2 1 1) and (2−2-1) surfaces for an oxygen reduction reaction. *Chem. Phys. Lett.* **2012**, *539*−*540*, 89−93.
(46) Ma, J.; Habrioux, A.; Luo, Y.; Ramos-Sanchez, G.; Calvillo, L.; Granozzi, G.; Balbuena, P. B.; Alonso-Vante, N. Electronic interaction between platinum nanoparticles and nitrogen-doped reduced graphene oxide: effect on the oxygen reduction reaction. *J. Mater. Chem. A* **2015**, *3* (22), 11891−11904.
(47) Zhang, L.; Xia, Z. Mechanisms of Oxygen Reduction Reaction on Nitrogen-Doped Graphene for Fuel Cells. *J. Phys. Chem. C* **2011**, *115* (22), 11170−11176.

DOI: 10.1021/acsami.7b14815
ACS Appl. Mater. Interfaces 2017, 9, 44519−44528